



The influence of microstructural evolutions on electrochemical corrosion and passive behavior in precipitation-strengthened high-entropy alloys

J.Y. Zhang^a, Y.H. Zhou^b, Z.Q. Ren^c, J.H. Luan^a, Y.L. Zhao^{c,*}, T. Yang^{a,d,e,*}

^a Department of Materials Science and Engineering, City University of Hong Kong, Hong Kong, China

^b Department of Mechanical Engineering, City University of Hong Kong, Hong Kong, China

^c School of Materials Science and Engineering, Harbin Institute of Technology, Shenzhen, China

^d City University of Hong Kong Shenzhen Research Institute, Shenzhen 518057, China

^e Hong Kong Branch of National Precious Metals Material Engineering Research Centre (NPMM), City University of Hong Kong, Hong Kong, China



ARTICLE INFO

Keywords:

High-entropy alloys
Microstructural evolutions
Corrosion behavior
Passive film
Micro-galvanic corrosion

ABSTRACT

Effects of microstructural evolutions on electrochemical corrosion properties and passive film characteristics of precipitation-strengthened $(\text{Ni}_2\text{Co}_2\text{FeCr})_{92}\text{Al}_4\text{Nb}_4$ high-entropy alloys (HEAs) were investigated in a saline environment. Compared with single-phase FCC alloys, the appearance of nano-sized L1_2 particles increases the metastable pitting activities and slightly reduces the pitting potential, while the lamellar D0_{19} phase further deteriorates the localized corrosion resistance. The chemical composition and oxide state of passive films are closely related to the different precipitation scenarios. The corrosion morphologies of the single-phase and L1_2 -strengthened alloys are dominated by pitting, whereas the intergranular corrosion (IGC) and intragranular dealloying-like corrosion occur in the D0_{19} -strengthened alloy.

1. Introduction

The environmental degradation of metals and alloys is termed corrosion, which is a ubiquitous failure mode in harsh environments [1, 2]. To prevent corrosion occurring, the corrosion-resistant alloys represented by traditional iron-based stainless steels (SS) and nickel-based superalloys are widely used in various corrosive environments such as oil, natural gas, power plants, and marine, enabling the construction of our metal-based civilization [3,4]. However, the traditional corrosion-resistant alloys dominated by one principal component (e.g., Fe or Ni) face severe challenges in satisfying advanced industrial applications in aggressive environments where high structural load-bearing capacity is concurrently required. That is to say, there is an urgent need for high-performance corrosion-resistant alloys with both high strength and good ductility [5]. Benefiting from the considerable compositional design space and tailorable phase structures, the new emerging HEAs exhibit numerous outstanding properties, such as good radiation resistance [6], desirable biocompatibility [7], and high strength and toughness [8]. In particular, the precipitation-strengthened HEAs with excellent comprehensive mechanical properties have recently gained increasing attention as a promising structural material

in the aqueous corrosion field [9–13]. For example, based on the beneficial effects of Ti and Nb on passivation, the recently designed Heusler-strengthened $(\text{CoCrFeNi})_{86}\text{Al}_7\text{Ti}_7$ HEA and L1_2 -strengthened $(\text{NiCo})_{77}\text{Cr}_{13}\text{Al}_5\text{Nb}_5$ HEA have been shown to possess excellent localized corrosion resistance in saline environments [10,11]. Precipitates in HEAs can inevitably cause micro-galvanic coupling due to the redistribution of elements between different phases, but how this specifically affects the electrochemical corrosion properties, and in particular the passive behavior, remains hitherto elusive.

The second phase in HEAs was initially introduced as an effective barrier to hinder the dislocation movement, thereby strengthening the alloy matrix. From the aqueous corrosion perspective, most of the microstructural transformations in HEAs are considered to deteriorate the corrosion resistance, which have been reported in FeCoNiCrAl_x (FCC to FCC+BCC) [14], $\text{FeCoNiCrCu}_{0.5}\text{Al}_x$ (FCC to FCC+BCC) [15], $\text{Fe}_{50}\text{Mn}_{25}\text{Cr}_{15}\text{Ni}_{10-x}\text{Co}_x$ (FCC to FCC+HCP) [16], and FeCoNiCrNb_x (FCC to FCC+Laves) HEAs [17]. In addition, AlCoCrFeNi_2 HEA with FCC+B2 dual-phase structure has also been demonstrated to have worse corrosion resistance than the CoCrFeNi_2 and CrFeNi_2 alloys with single-phase FCC structure [18]. Ayyagari et al. compared the corrosion performance of aged and recrystallized $\text{Al}_{0.3}\text{Cu}_{0.3}\text{Ti}_{0.2}\text{CoCrFeNi}$ HEAs in

* Corresponding author.

* Corresponding author at: Department of Materials Science and Engineering, City University of Hong Kong, Hong Kong, China.

E-mail addresses: zhaoyilu@hit.edu.cn (Y.L. Zhao), taoyang6-c@my.cityu.edu.hk (T. Yang).

a 3.5 wt% NaCl solution and found that the presence of L1₂, Heusler, and Cu-rich phases in the aged alloys reduced the corrosion resistance and increased the metastable pitting activities during the anodic polarization stage [19]. The galvanic corrosion between these precipitates and the substrate was considered to be the main reason for the deterioration of electrochemical performance, but they did not give the passive film changes associated with the precipitates [19]. Alternatively, there are also some scenarios that phase transformations can improve the corrosion resistance of HEAs, such as the Al_{0.3}Cr_xFeCoNi (FCC to FCC+BCC) with increasing Cr content [20] and NiCoVAL_x (FCC to FCC+B2) with increasing Al content [21]. A recent study has shown that aging-treated AlCoCrFeNi_{2.1} HEAs exhibit superior corrosion resistance to their solution-treated counterparts, which is due to the effective passive films promoted by the phase decomposition of the eutectic structure into L1₂/FCC and B2/BCC [22]. The above studies indicate that the effect of precipitates on the electrochemical corrosion performance and passive film characteristics of HEAs still needs to be carefully studied.

More recently, we have discovered that the temperature-dependent microstructural evolutions have a decisive impact on the mechanical properties in (Ni₂Co₂FeCr)₉₂Al₄Nb₄ HEA (at%, denoted as the Al4Nb4), with L1₂-strengthened alloys having superior comprehensive mechanical properties than the D0₁₉-strengthened alloys [23]. However, as of now, the electrochemical response of this HEA containing different precipitates (L1₂ phase or D0₁₉ phase) has yet to be discovered. Therefore, in order to investigate the impact of the L1₂ phase and D0₁₉ phase on the corrosion performance of the Al4Nb4 HEA, we selected 700 °C and 900 °C aged alloys without other heterogeneous phases for comparison with the recrystallized ones in a precipitate-free state. The potentiodynamic polarization and electrochemical impedance spectroscopy (EIS) tests were used to evaluate the electrochemical corrosion properties of the alloys. X-ray photoelectron spectroscopy (XPS) and Cs-corrected scanning transmission electron microscopy high-angle annular dark-field (STEM-HAADF) imaging were used to characterize the composition, structure, and thickness of the passive film on the alloy surface. The scanning Kelvin probe force microscopy (SKPFM) was used to detect the possible micro-galvanic tendency in alloys. A fundamental understanding of the corrosion-mechanics-structure-composition relationship can enable us to design precipitation-strengthened HEAs with high strength, appreciable ductility, and superior corrosion resistance.

2. Experimental procedures

2.1. Alloys fabrication

The investigated alloy with a nominal composition of (Ni₂Co₂FeCr)₉₂Al₄Nb₄ was prepared by arc melting in a high-purity argon atmosphere. The arc-melted ingots were repeatedly turned over and remelted at least 6 times to ensure thorough mixing of all elements (purity greater than 99.9 wt%), and then drop cast into a copper mold with a dimension of 5 × 12 × 100 mm³. After that, the as-cast ingots were homogenized at 1200 °C for 2 h to further eliminate compositional and microstructural inhomogeneities, and then cold-rolled along the longitudinal direction, resulting in a total thickness reduction of ~65%. Subsequently, the cold-rolled specimens were recrystallized at 1200 °C for 1.5 min to obtain a single-phase alloy with an average grain size of ~50 μm. The single-phase structure was confirmed by a micro-hardness tester. Based on our previous studies, the recrystallized alloys were aged at 700 °C and 900 °C for 32 h, respectively, to obtain different types of precipitates [23]. The above heat treatment processes were carried out in the air and ended with air cooling.

2.2. Electrochemical and corrosion immersion tests

The electrochemical measurements were conducted in 3.5 wt% NaCl solution at room temperature using a standard three-electrode cell with the Al4Nb4 HEA as the working electrode, a saturated calomel electrode

(SCE) as the reference electrode, and a Pt foil as the counter electrode. The electrochemical data were collected on an electrochemical workstation (CHI 760E). The adopted electrolyte was prepared by reagent grade NaCl and deionized water with a resistivity of ~18.25 MΩ·cm. The working electrode was machined into a 14-mm-diameter disc and mounted in a Teflon holder to provide an exposed area of 1 cm². The surface of these coupons was ground to 5000-grit, then polished using a 1 μm suspension, and finally rinsed with deionized water and ultrasonically vibrated in alcohol for 3 min. To minimize the interference from air oxidation, the polished specimens were dried in a low stream of nitrogen gas and stored in a portable vacuum chamber until the electrochemical testing. To ensure the stability of the electrochemical system: (i) the electrochemical cell was placed inside a Faraday cage, (ii) the reference electrode was connected to the cell via a Luggin capillary, and (iii) the area of the selected counter electrode was larger than that of the working electrode. Before starting the tests, the working electrode was cathodically polarized at -0.8 V_{SCE} for 5 min to remove any air-formed film, and then monitored at an open circuit potential (OCP) for 1 h to obtain a stable surface state. Subsequently, this surface state was analyzed by electrochemical impedance spectroscopy (EIS), by applying a sinusoidal alternating current (AC) potential with an amplitude of 10 mV and a frequency ranging from 100 kHz to 10 mHz to the working electrode. The frequency-dependent electrical current response was analyzed by the Zview software and fitted using an equivalent electrical circuit (EEC). The potentiodynamic polarization tests were performed at a scan rate of 1 mV/s from -0.6 V_{SCE} towards the anodic direction until a sudden increase in current. In order to investigate the effect of microstructural evolutions on the electrochemical corrosion morphology, the specimens were potentiostatically polarized at 1 V_{SCE} (above the pitting potential) for 3 min, and then ultrasonically cleaned with alcohol for 5 min. In addition, the specimen aged at 900 °C was selected for corrosion immersion testing, which was immersed in 2 M NaCl + 0.05 M HCl solution at 37 ± 0.5 °C for 12 h to analyze galvanic corrosion activities caused by the intense elemental partitioning. At least four specimens were tested for each microstructural condition to ensure the data reproducibility.

2.3. Microstructural characterization

A scanning electron microscope (SEM, Quanta FEG450, FEI) equipped with an electron back-scattered diffraction (EBSD) detector was used to characterize the temperature-dependent microstructural evolutions. The specimens for SEM and EBSD were sequentially mechanically ground, polished, and then electropolished using a nitric acid-alcohol mixed solution (nitric acid: alcohol = 1:3) according to the standard metallographic techniques. The crystal structure of alloys and the chemical composition of the constituent phases were identified by a transmission electron microscope (TEM, 2100 F, JEOL) equipped with an energy dispersive spectrometer (EDS). The specimens used for TEM observations were first ground to a thickness of ~50 μm, then mechanically dimpled and ion-thinned using a precision ion polishing system (PIPS, Model 695, Gatan) until electron-penetrable thickness. Atom probe tomography (APT) was used to analyze the compositional distribution of the specimen on a near-atomic scale. The tip-shaped specimen for APT test was prepared using focused ion beam/scanning electron microscope (FIB/SEM, FEI) dual-beam system with a Ga⁺ source. APT testing was performed on a local electrode atom probe (LEAP, 5000XR, CAMECA) under high vacuum and cryogenic conditions with a 20% pulse fraction and a 200 kHz pulse rate. APT raw data were collected and analyzed using the commercial software package IVAS 3.8.4, and the reconstruction parameters were calibrated according to the crystallographic features on the detector hit map [24].

The chemical state within the passive film on the specimen surface was characterized by XPS (Escalab Xi⁺, Thermo Scientific) with a monochromatized Al Kα X-ray source (1486.6 eV). The passive films were obtained by potentiostatic polarization in 3.5 wt% NaCl solution at

0.2 V_{SCE} (in the passive region) for 2 h. After the growth of the passive film was completed, the specimens were immediately taken out and cleaned with deionized water, and then dried under a flowing nitrogen gas. A portable vacuum container was used to move the specimen directly into the XPS vacuum transfer chamber to prevent direct air exposure. The chamber was kept at a pressure of $\sim 10^{-8}$ Torr during the characterizations. The XPS testing consists of a survey spectrum and several high-resolution spectra, where the high-resolution spectra are collected on the Ni 2p, Co 2p, Fe 2p, Cr 2p, Al 2p, Nb 3d, and O 1s core series based on the corresponding binding energy intervals obtained by the initial survey scans. The chemical shifts of all spectra were calibrated according to the well-known binding energy of adventitious alkyl (C-C) peak at 284.8 eV. After subtracting a Shirley background profile, the high-resolution spectra were fitted with the Voigt function based on the known reference compounds using Avantage software. Cation fractions within the passive film are determined by the peak area corresponding to the specific oxide state. XPS tests were conducted at four random locations for each specimen. To further characterize the thickness, composition, and structure of the passive film, the cross-sectional passive films were prepared by FIB. A 12-nm-thick Au protective layer was

pre-deposited on the specimen surface using vacuum sputtering equipment (Smart Coater, JEOL) to prevent Ga ions from damaging the passive film. Then, the thin foil of passive films was characterized by a scanning transmission electron microscopy (STEM, Talos F200X, FEI) equipped with a super-X EDS detector. The atomic-scale characterization of passive films was obtained by the double aberration-corrected TEM (Titan Cubed Themis G2 300, FEI). Finally, to measure the pitting corrosion depth and galvanic corrosion tendency, the surface morphologies after electrochemical testing and immersion corrosion were observed by confocal laser scanning microscopy (CLSM, VK-X3000, Keyence).

2.4. Volta potential measurement

In order to evaluate the galvanic corrosion tendency due to elemental segregation, the SKPFM was used to detect the Volta potential difference of alloys aged at 900 °C. SKPFM tests were performed on an atomic force microscope (AFM, MFP-3D Infinity, Oxford). An electrically conductive Pt-coated silicon tip (MikroMasch, XSC11) with a known work function was used to probe the surface topography and

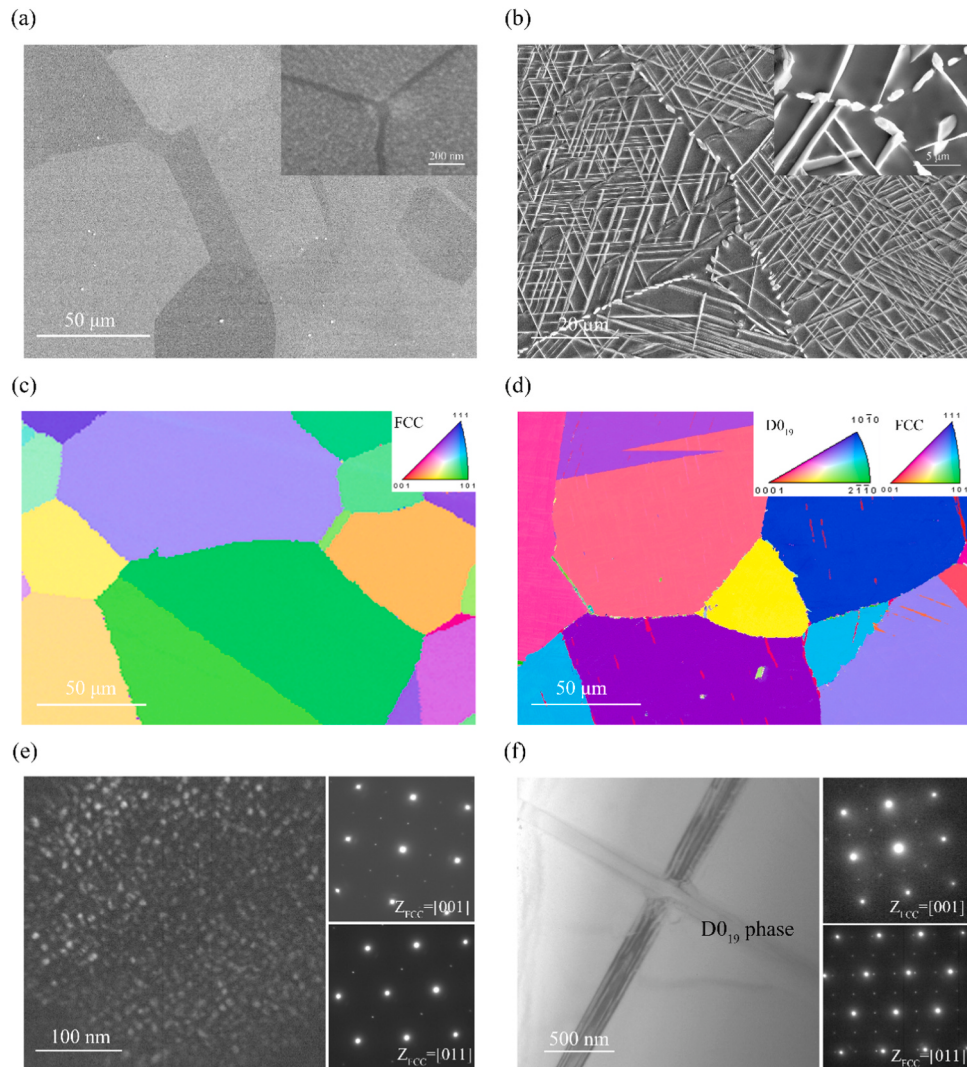


Fig. 1. Microstructural evolutions of the Al4Nb4 HEAs at different aging temperatures. SEM images of Al4Nb4 alloy aged at (a) 700 °C for 32 h and (b) 900 °C for 32 h. The insets in (a) and (b) are magnified views of the corresponding grain boundaries. EBSD IPF images of Al4Nb4 alloy aged at (c) 700 °C for 32 h and (d) 900 °C for 32 h. (e) A dark-field TEM image of Al4Nb4 alloy aged at 700 °C for 32 h, showing dense nano-sized L1₂ particles uniformly distributed within the FCC matrix. The SADPs from the [001] axis and [011] axis of the matrix on the right-hand side indicate that the orientation relationship between the L1₂ phase and the FCC matrix is $<110>\{111\}_{L1_2} // <110>\{111\}_{FCC}$. (f) A bright-field TEM image of Al4Nb4 alloy aged at 900 °C for 32 h and SADPs from the [001] axis and [011] axis of the matrix. The orientation relationship between the D0₁₉ phase and FCC matrix is $<11\bar{2}0>\{0001\}_{D0_{19}} // <110>\{111\}_{FCC}$.

Volta potential map of the alloy simultaneously. The specimens used for SKPFM were polished and then immersed in 2 M NaCl + 0.05 M HCl solution for 12 h. Afterward, they were ultrasonically cleaned with alcohol to obtain a fresh surface and stored in a vacuum container. The SKPFM tests were conducted at room temperature, with the relative air humidity controlled below 40% to avoid excessive adsorbed water film on the surface. The Volta potential difference obtained by SKPFM testing has been reported to reflect the galvanic features between two phases, with regions of higher potential usually having more stable electrochemical stability.

3. Results and discussion

3.1. Microstructural and compositional changes upon aging

The temperature-dependent microstructural characteristics of Al4Nb4 HEA are presented in Fig. 1, in which the Fig. 1(a, c, e) and Fig. 1(b, d, f) show mesoscale to nanoscale microstructural observations of the specimens aged at 700 °C and 900 °C for 32 h, respectively. The SEM image in Fig. 1(a) shows that the specimen aged at 700 °C has a typical polycrystalline morphology, similar to the recrystallized one (not shown here), and the clean grain boundaries without other

heterogeneous precipitates are identified within the corresponding inset. In sharp contrast, numerous intersected Widmanstätten-type lath-like precipitates and a continuous distribution of irregular precipitates on the grain boundaries were observed in the specimen aged at 900 °C, as shown in Fig. 1(b). The inset in Fig. 1(b) further shows that part of the lamellar precipitates are originated from the irregular particles on the grain boundaries and extended into the grains. The EBSD inverse pole figure (IPF) images in Fig. 1(c) and (d) indicate that the two aged alloys have similar grain sizes, and the lamellar precipitates are found to have different crystal orientations with the matrix. The EBSD image quality (IQ) and phase map (Fig. S1) demonstrate that the precipitates within the grains and on the grain boundaries are a Ti₃Al-type phase with the D0₁₉ structure. A representative dark-field TEM image of the specimen aged at 700 °C and the corresponding selected-area diffraction patterns (SADPs) from the [001] and [011] zone axes are presented in Fig. 1(e). The uniform distribution of dense nano-sized particles within the alloy matrix and the superlattice diffractions (weak spots) in the SADPs simultaneously demonstrate that the nanoparticles are a Ni₃Al-type phase with an L1₂ structure. The orientation relationship between the L1₂ phase and the FCC matrix is <110>{111}_{L1₂}//<110>{111}_{FCC}. Fig. 1(f) presents a bright-field TEM image of the specimen aged at 900 °C containing the intersected lamellar D0₁₉ phase, and the average

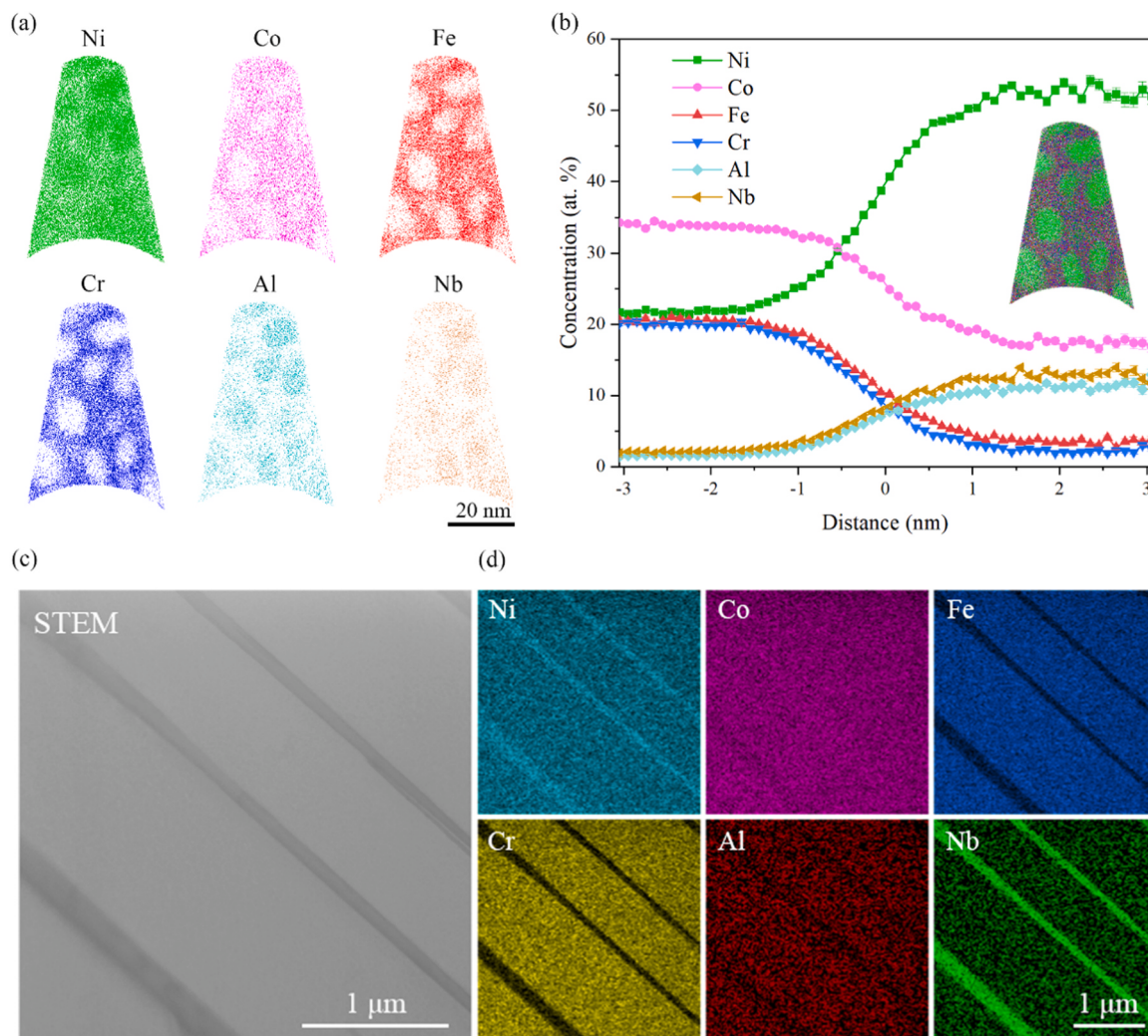


Fig. 2. The detailed compositional analysis of Al4Nb4 alloys at different aging temperatures. (a) Atom maps of Ni, Co, Fe, Cr, Al, and Nb of the alloy aged at 700 °C, showing that Ni, Al, and Nb are enriched in the L1₂ particles, while the FCC matrix is enriched in Co, Fe, and Cr. (b) Composition profiles across the interfaces between L1₂ particles and FCC matrix, with the inserted 3D atomic reconstruction map, showing detailed compositional differences between the two phases. (c) STEM image and (d) corresponding compositional distributions of the alloy aged at 900 °C, showing that the D0₁₉ phase is enriched in Ni and Nb, while depleted in Fe and Cr. The Co element has no visible segregation behavior.

thickness of the D₀₁₉ phase was statistically estimated to be \sim 74 nm. The corresponding SADPs from the [001] and [011] zone axes indicate that there is a semi-coherent relationship between the D₀₁₉ phase and the matrix, and the orientation relationship between them is $<11\bar{2}0>\{0001\}_{D0_{19}}//<110>\{111\}_{FCC}$.

Due to the existence of nano-sized L₁₂ particles, the compositional partitioning behavior between the two phases (*i.e.*, disordered FCC phase and ordered L₁₂ phase) in the 700 °C aged specimen is characterized by APT, as shown in Fig. 2(a) and (b). Fig. 2(a) shows the atom maps of all elements. The L₁₂ particles enriched with Ni, Al, and Nb can be clearly identified, while the Fe, Co, and Cr elements are partitioned into the surrounding FCC matrix. The compositional distribution between the L₁₂ phase and the matrix is quantitatively summarized in Fig. 2(b), where the L₁₂ phase contains 52% Ni, 18% Co, 11% Al, 13% Nb (at%), and a trace amount of Fe and Cr, suggesting its multi-component compositional characteristic close to the stoichiometric ratio of (Ni, Co, Fe, Cr)₃(Al, Nb) [25]. In addition, the interface between the two phases is defined by the 35 at% Ni iso-concentration surface, as shown in the 3D atomic reconstruction map (inset of Fig. 2(b)). Fig. 2(c) and (d) show the STEM image and the corresponding elemental maps of the specimen aged at 900 °C, respectively. The lamellar D₀₁₉ phase was

found to have a different partitioning behavior from the L₁₂ particles, in which the Ni and Nb are strongly partitioned into the D₀₁₉ phase, Fe, Cr, and Al elements are severely deficient, while the Co element has no obvious partitioning preference. It can be inferred that the D₀₁₉ phase has a chemical composition close to (Ni, Co)₃Nb. Compared to the recrystallized single-phase Al₄Nb₄ alloy that is a homogeneous solid solution, the different precipitation scenarios in the aged alloys can inevitably change the electrochemical corrosion properties and the associated passive behavior, which we will discuss in detail next.

3.2. Electrochemical corrosion properties

The electrochemical corrosion behavior of Al₄Nb₄ HEAs was studied in 3.5 wt% NaCl solution at room temperature. Fig. 3(a) shows the potentiodynamic polarization curves of three Al₄Nb₄ HEAs with different structures (single-phase FCC, FCC+L₁₂, and FCC+D₀₁₉). At first glance, the three alloys share similar cathodic and anodic polarization processes and lack the active-to-passive current transitions, suggesting that they all have the ability to spontaneously passivate at OCP [26]. A significant difference is their localized corrosion resistance, reflected in their different passive regions and metastable pitting activities, as shown in the inset of Fig. 3(a). The electrochemical parameters,

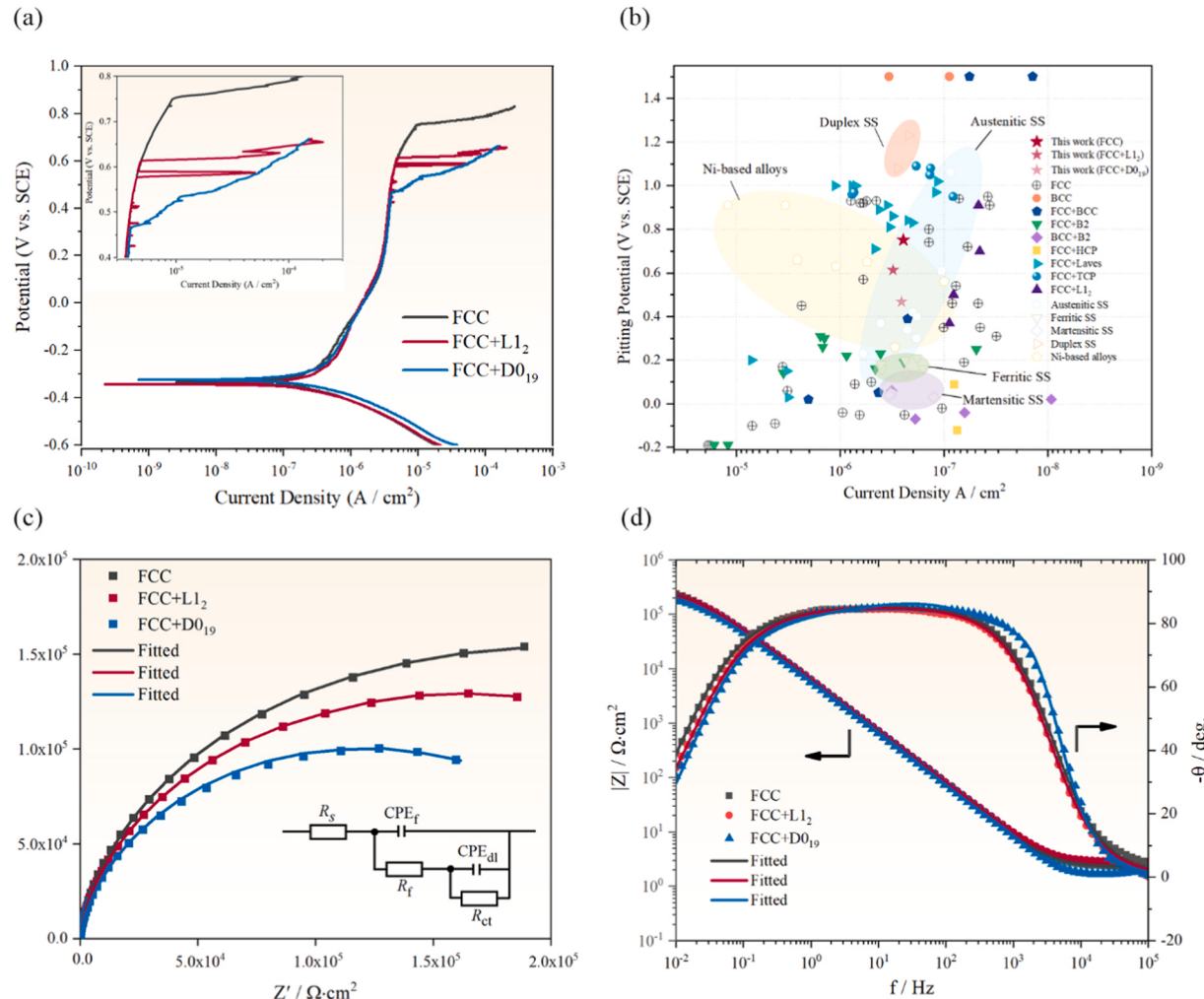


Fig. 3. Effect of microstructural evolutions on the electrochemical behavior of Al₄Nb₄ HEAs in 3.5 wt% NaCl solution at room temperature. (a) Potentiodynamic polarization curves of Al₄Nb₄ alloys in the recrystallized state (single-phase FCC structure), 700 °C aged state (FCC+L₁₂ structure), and 900 °C aged state (FCC+D₀₁₉ structure). The inset shows the effect of different precipitates on metastable pitting events and the E_{pit} . (b) E_{pit} versus i_{corr} between Al₄Nb₄ HEAs and other corrosion-resistant alloys in 3.5 wt% NaCl solution at room temperature. (c) EIS Nyquist plots of these three alloys, with the inset showing an equivalent electrical circuit (EEC) model used to fit the EIS data. The fitted curves are shown as solid lines. (d) EIS Bode plots for these three alloys. Z' and $Z̄$ represent the real and imaginary impedance, respectively. $|Z|$ is the impedance modulus, and θ is the phase shift of the electrochemical system.

including corrosion current density (i_{corr}), corrosion potential (E_{corr}), and pitting potential (E_{pit}), were calculated and summarized in Table 1. The i_{corr} is obtained by the Tafel extrapolation method based on the Butler-Volmer equation [27],

$$i = i_{corr} \left\{ \exp \left[\frac{2.303(E - E_{corr})}{\beta_a} \right] - \exp \left[\frac{2.303(E - E_{corr})}{\beta_c} \right] \right\} \quad (1)$$

where i is the external current density, E is the applied potential, and β_a and β_c are the Tafel slopes of the anodic and cathodic branches, respectively. E_{corr} and E_{pit} correspond to the potentials at the minimum corrosion current and the sudden increase in corrosion current, respectively [28]. From Fig. 3(a) and Table 1, the different microstructures have no significant impact on the i_{corr} and E_{corr} of Al4Nb4 alloys, but mainly change the localized corrosion resistance, i.e., the E_{pit} . Specifically, the single-phase FCC alloy has the most superior localized corrosion resistance, as reflected in its highest E_{pit} of approximately 751 mV_{SCE}. After aging at 700 °C, the E_{pit} of L1₂-strengthened alloy dropped to 614 mV_{SCE} and was accompanied by some pronounced anodic current peaks (an indicator of metastable pitting events) occurring close to the transpassive dissolution region. Aging at a higher temperature (900 °C) resulted in the lowest E_{pit} for the D0₁₉-strengthened alloy (~468 mV_{SCE}), indicating that the passive film formed during the anodic scanning process is more vulnerable to chloride ion attacks and prone to earlier localized dissolution. Nevertheless, it is worth noting that under the same corrosive environments, both the single-phase FCC and L1₂-strengthened Al4Nb4 HEAs have comparable corrosion resistance to traditional corrosion-resistant alloys [9] and higher E_{pit} than most of the HEAs reported so far, such as eutectic AlCoCrFeNi_{2.1} HEAs [22], NiCoV medium-entropy alloys [21,29], Cantor alloy [30], and FeCoNiCrAl_x HEAs [31], as shown in Fig. 3(b). In addition, based on our previous research and Fig. S2, we find that the L1₂-strengthened Al4Nb4 HEA has the most excellent comprehensive mechanical properties and aqueous corrosion resistance compared to the single-phase FCC and D0₁₉-strengthened counterparts.

In order to verify the intrinsic protective properties of the passive film on the Al4Nb4 alloy with different microstructural characteristics, the EIS tests were conducted under OCP. Fig. 3(c) shows the representative Nyquist impedance spectra of the three Al4Nb4 HEAs with different structures. All three alloys exhibit typical near-capacitive response in the whole-frequency region, as reflected in their depressed semicircle features. Generally, a larger semicircle radius indicates that the passive film formed on the alloy surface is more effective in resisting charge transfer reactions, i.e., more electrochemically stable [32]. Therefore, the passive film stability of the single-phase FCC alloy is better than that of the L1₂-strengthened alloy, while the D0₁₉-strengthened alloy has the lowest passive film stability, which is consistent with the results of the potentiodynamic polarization tests (Fig. 3(a)). The frequency-dependent EIS response is further reflected in the Bode plots (Fig. 3(d)), showing the variation of impedance modulus ($|Z|$) and phase angle (θ) relative to the frequency. In the mid-frequency intervals (10^3 – 10^{-1} Hz), the slope of $\log |Z|$ against $\log f$ is close to -1 , and the θ is close to the maximum value of -90 degrees, both of which indicate that the alloy surface passive film is close to the characteristics of an ideal capacitor [33]. In addition, the low-frequency impedance modulus values (e.g., at 10^{-1} Hz) have been reported to evaluate the relative protective properties of passive films, with larger modulus

values indicating more stable passive films [34,35]. As can be seen from Fig. 3(d), the FCC and L1₂-strengthened alloys tend to form more stable passive films in saline environments, resulting in higher modulus values than the D0₁₉-strengthened counterparts.

By fitting the EIS data, we can quantitatively analyze the protective properties of the passive films. The inset in Fig. 3(c) is the EEC used to fit the EIS data, where R_s represents the solution resistance, R_f is the passive film resistance, R_{ct} is the charge transfer resistance occurring on the solution/film interface. CPE is the constant phase element, where CPE_f is the passive film capacitance and CPE_{dl} represents the double-layer capacitance. The fitting parameters are summarized in Table 2, and the fitted curves are shown as solid lines. The fitting reliability is guaranteed by the minimal χ^2 values ($\sim 10^{-4}$, order of magnitudes). During the EIS testing, the electrochemical system essentially mirrors the behavior of the solution resistance in the high-frequency region due to the near-capacitive characteristics of passive films. Therefore, the impedance modulus of the three HEAs is about $2 \Omega \cdot \text{cm}^2$ at 10^5 Hz, and the corresponding phase angle is basically zero. R_{ct} is a critical parameter in passive alloys with its value equals to the radius of the semicircle in Nyquist plots, and can be well used to evaluate the compactness and stability of the alloy passive films [36]. The FCC alloy has the highest R_{ct} value, followed by the L1₂-strengthened alloy, and the D0₁₉-strengthened alloy has the lowest R_{ct} value. These results indicate that the intense elemental partitioning behavior leads to a decrease in the stability of the passive film. CPE is used to quantitatively characterize the near-capacitive response of the three alloys, which is defined as $Z_{CPE} = \frac{1}{Y_0} (j\omega)^{-\alpha}$ [37]. Y_0 is a proportional factor, $j = \sqrt{-1}$, ω is the angular frequency ($\omega = 2\pi \times f$), and α is an exponent (for an ideal capacitor, $\alpha = 1$, and for CPE, $0 < \alpha < 1$). Z_{CPE} can also be expressed as $Z_{CPE} = \frac{1}{Y_0} \omega^{-\alpha} (\cos \frac{\alpha\pi}{2} - j \sin \frac{\alpha\pi}{2})$, which explains the characteristics of the depressed semicircle in the Nyquist plots [9]. From Table 2, the α values of passive films of the three alloys are around 0.95, which is due to the surface roughness or other superficial phenomena that cause the surface passive film to deviate from the ideal capacitor ($\alpha = 1$) [38]. In short, the polarization tests and EIS results demonstrate that the single-phase FCC Al4Nb4 alloy has superior corrosion resistance, and the microstructural evolutions affect the stability of the passive film, thereby changing the electrochemical corrosion behavior.

3.3. XPS characterization of passive films

It is widely documented that surface nanoscale passive films play a decisive role in the corrosion resistance and electrochemical corrosion behavior of alloys [39,40]. XPS was used to investigate the chemical composition and metallic oxidation state of the potentiostatically grown passive films of Al4Nb4 HEAs with different structures, and the chosen fixed potential (0.2 V_{SCE}) was determined based on the results of previous potentiodynamic polarization tests. Fig. 4(a-g) show the high-resolution spectra of individual constituent elements (including O 1 s) of the passive film on the surface of the single-phase FCC alloy. Except for Ni, which is decomposed into mainly metallic Ni (Ni⁰), other elements exist in the passive film as their own oxides or hydroxides. For example, the oxides or hydroxides of Co and Fe are the main components of Co 2p_{3/2} and Fe 2p_{3/2}, respectively. Cr₂O₃ dominates Cr 2p_{3/2}, and the Al 2p and Nb 3d are divided into significant amounts of Al₂O₃ and Nb₂O₅, respectively. The detailed cationic and metallic fractions are calculated based on the corresponding XPS peak areas and are displayed in Fig. 4(h), with the relative percentages of each element marked. Evidently, iron oxides (FeO and Fe₂O₃) and Cr₂O₃ are the main components of the passive film, followed by Al₂O₃ and Nb₂O₅. Trace amounts of Co and Ni oxides were observed in the passive film. The iron oxides and hydroxides present in the passive films are generally considered ionically and electronically conductive, making them difficult to effectively protect the alloy matrix [41]. Therefore, the wide passive region and excellent localized corrosion resistance of the

Table 1

The common electrochemical parameters of Al4Nb4 HEAs with single-phase FCC structure, FCC+L1₂ dual-phase structure, and FCC+D0₁₉ dual-phase structure obtained in 3.5 wt% NaCl solution.

Al4Nb4 HEA	E_{corr} (mV _{SCE})	i_{corr} (nA/cm ²)	E_{pit} (mV _{SCE})
FCC	-335 ± 17	247.5 ± 9	751 ± 16
FCC+L1 ₂	-343 ± 20	311.2 ± 13	614 ± 24
FCC+D0 ₁₉	-324 ± 33	258.6 ± 36	468 ± 28

Table 2

EEC fitting parameters for the Al4Nb4 HEAs with different structures in 3.5 wt% NaCl solution under OCP.

Al4Nb4 HEA	R_s ($\Omega \cdot \text{cm}^2$)	R_f ($10^5 \cdot \Omega \cdot \text{cm}^2$)	R_{ct} ($10^5 \cdot \Omega \cdot \text{cm}^2$)	CPE _f	CPE _{dl}		
				Y_0 ($10^{-5} \cdot \Omega^{-1} \cdot \text{cm}^{-2} \cdot \text{sec}^\alpha$)	α	Y_0 ($10^{-5} \cdot \Omega^{-1} \cdot \text{cm}^{-2} \cdot \text{sec}^\alpha$)	α
FCC	2.29	1.39	2.73	2.94	0.95	0.83	0.49
FCC+L1 ₂	2.80	1.30	2.43	2.74	0.95	0.94	0.44
FCC+D0 ₁₉	1.82	1.24	1.31	2.89	0.95	1.21	0.75

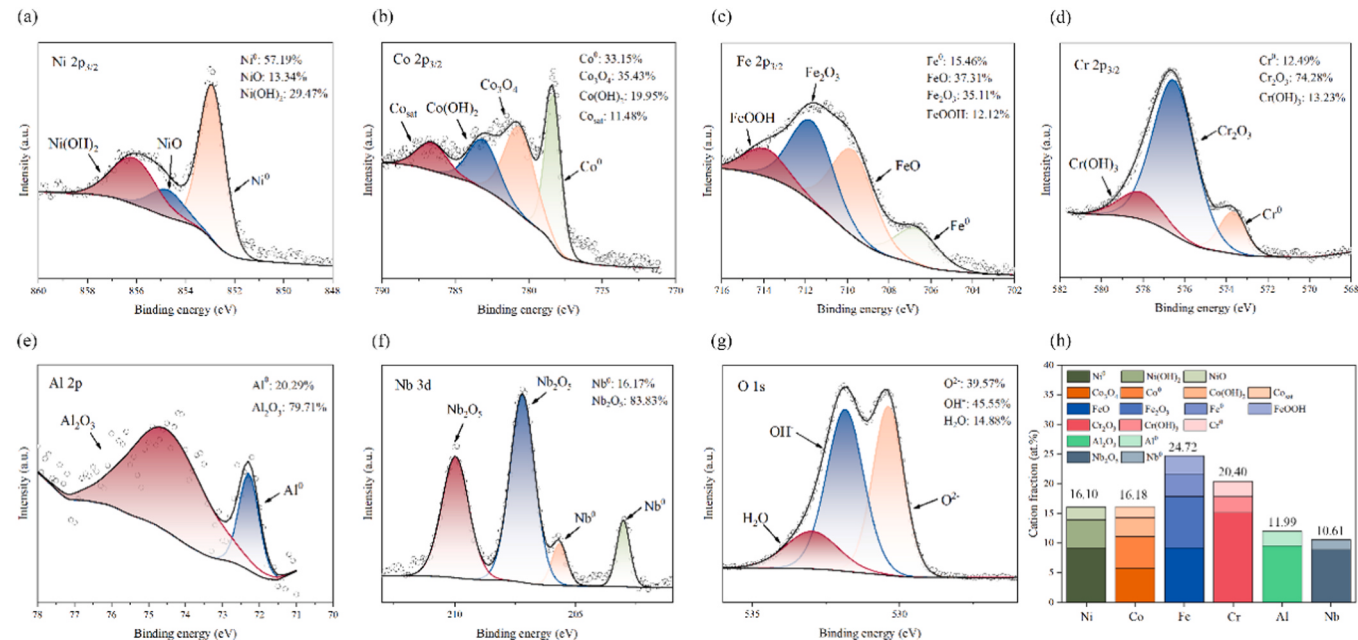


Fig. 4. XPS analysis of the potentiostatically grown passive film on the recrystallized Al4Nb4 alloy (single-phase FCC structure) surface after fixing the potential at 0.2 V_{SCE} for 2 h in 3.5 wt% NaCl solution. High-resolution spectra of (a) Ni 2p_{3/2}, (b) Co 2p_{3/2}, (c) Fe 2p_{3/2}, (d) Cr 2p_{3/2}, (e) Al 2p, (f) Nb 3d, (g) O 1 s. (h) Cationic fractions in the passive film, with their relative percentage marked.

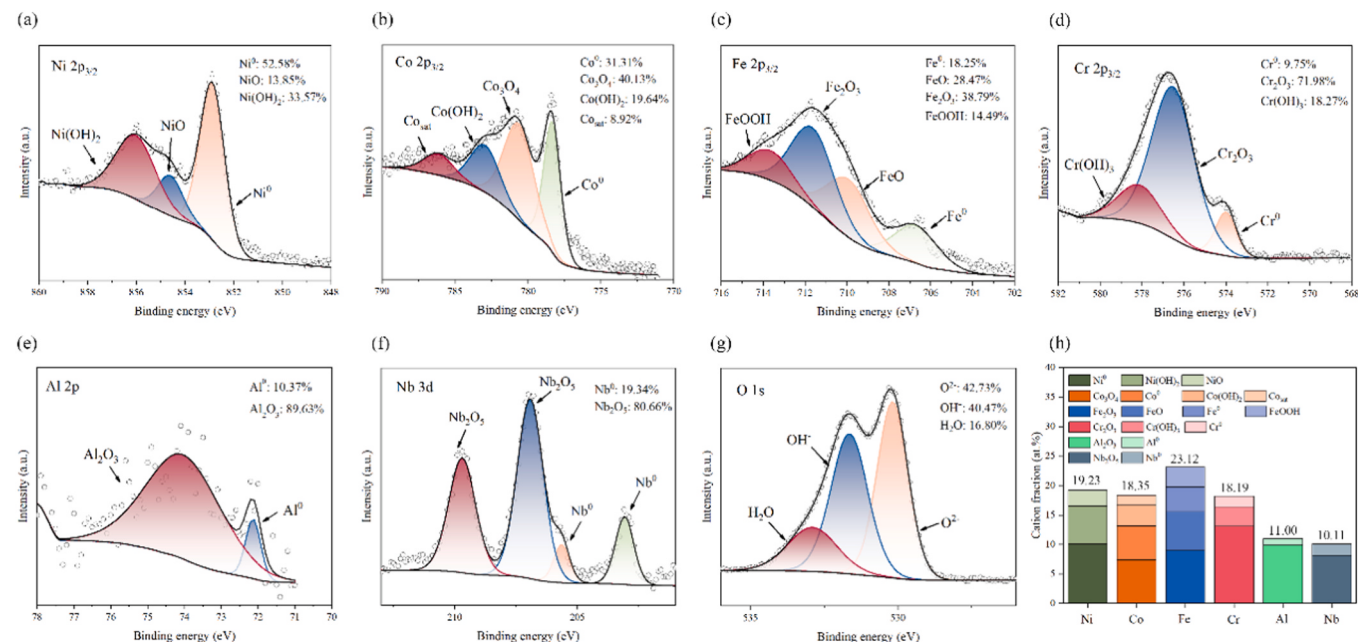


Fig. 5. XPS analysis of the passive film (potentiostatic polarization at 0.2 V_{SCE} in 3.5 wt% NaCl solution for 2 h) on the Al4Nb4 alloy aged at 700 °C (FCC+L1₂ structure). High-resolution spectra of (a) Ni 2p_{3/2}, (b) Co 2p_{3/2}, (c) Fe 2p_{3/2}, (d) Cr 2p_{3/2}, (e) Al 2p, (f) Nb 3d, (g) O 1 s. (h) Cationic fractions in the passive film, with their relative percentage marked.

single-phase FCC alloys are mainly attributed to the large amount of Cr_2O_3 present in the passive film. The Al4Nb4 HEAs contains 15.33 at% Cr, which exceeds the Cr content threshold (12 at%) for traditional stainless steels that can form a Cr_2O_3 -based passive film [42]. In addition, Nb_2O_5 and small amounts of Al_2O_3 have also been reported to enhance the stability and robustness of passive films [43,44].

After aging at 700 °C, the effect of the appearance of nano-sized L1₂ particles on the passive film is shown in Fig. 5. Iron oxides and Cr_2O_3 are still the main constituents of the passive film. Ni, Co, Al, and Nb maintain the same peak splitting and similar cationic ratios as their counterparts in the single-phase FCC alloy. Given their similar surface passivation characteristics, L1₂-reinforced alloys have comparable corrosion resistance to that of the FCC alloys. However, it is worth noting that there is a slight decrease in the proportion of Cr_2O_3 compared to the FCC alloy, which may explain the apparent metastable pitting activities in the late passivation region of the L1₂-strengthened alloy (Fig. 3(a)). A drastic change in the surface passive film was observed in the D0₁₉-strengthened alloy, as shown in Fig. 6. Fe and Cr are no longer the main constituents in the passive film and are replaced by Co and Ni. The percentage of Cr is further reduced to 13.44%, and the fraction of Cr_2O_3 is also reduced compared to that of the FCC and L1₂-strengthened alloys. This suggests that the dense distribution of lamellar D0₁₉ phase with (Ni, Co)₃Nb composition on the alloy surface makes it difficult for the 900 °C aged alloy to form a stable passive film mainly composed of Cr_2O_3 , which further leads to a premature localized disruption of the passive film. It is also noteworthy that the O 1 s peak on the surface of the D0₁₉-strengthened alloy is separated into two components: O²⁻ (530.1 eV) and OH⁻ (531.8 eV), and the OH⁻ species occupy a dominant position. Compared to the O 1 s peak in the single-phase FCC alloy (Fig. 4(g)) and FCC+L1₂ dual-phase alloy (Fig. 5(g)), the FCC+D0₁₉ dual-phase alloy accounts for more OH⁻ species and lacks the third peak representing bound water (H_2O). Hydroxide-dominated passive films are generally considered to be electrochemically unstable compared to the corresponding oxide-dominated ones, leading to an earlier degradation of the passive films on D0₁₉-strengthened alloy [45]. At the same time, the absence of bound water also reduces the ability of the passive film to capture dissolved metal ions, making it difficult to form a compact passive film, and thus contributing to its vulnerability to

corrosive ion attacks [46]. A similar scenario was reported in a study comparing the aqueous corrosion behavior of Cantor alloy with 304 SS, where Luo et al. found that the hydroxide-dominated passive film and the absence of bound water resulted in inferior corrosion performance of Cantor alloy compared to 304 SS in 0.1 M H_2SO_4 solution [34].

3.4. STEM analysis of passive films

In order to obtain detailed information about the passive film, e.g., the chemical composition, thickness, and structure, the passive film formed on the surface of the L1₂-strengthened alloy (the excellent combination of mechanical and corrosion properties) was carefully analyzed by STEM and atomic resolution STEM-HAADF. Fig. 7(a) shows the STEM image of the cross-sectional passive film potentiostatically grown on the surface of the L1₂-strengthened alloy. Before depositing Pt, a 12-nm-thick Au layer was pre-deposited on the sample surface to protect the passive film from Ga^+ damage. Therefore, from top to bottom in Fig. 7(a), the Pt layer, the Au layer, the nanoscale passive film, and the alloy matrix can be observed in sequence. The passive film is clearly visible as a continuous and straight interfacial layer on the alloy substrate, and the average thickness of which is counted as ~3.5 nm. The integrated STEM line scan analysis from the red rectangle outlined in Fig. 7(a) is shown in Fig. 7(b). The intense oxygen peak first confirmed the existence of an oxygen-enriched passive film. In addition, the passive film was found to be enriched in Fe and Cr, while containing relatively small amounts of Ni and Co, which is in good agreement with the XPS results (Fig. 5). More importantly, Fe in the passive film tends to accumulate in the outer layer, while Cr is mainly distributed in the inner layer. This bilayered passive film can be more clearly observed in Fig. 7(c) and is schematically illustrated in Fig. 7(d). The Cr-rich inner layer is tightly bonded to the substrate, providing inherent protective properties against further attacks from the surrounding environment.

Fig. 8 shows the STEM mapping of a cross-sectional passive film containing Pt, Au, O, and individual alloying elements. The passive film layer, which is a mixture of various oxides and hydroxides, can be distinguished in the O elemental map. The duplex passive film with a Fe-rich outer layer and a Cr-rich inner layer can also be observed in the Fe and Cr elemental maps, respectively. These findings are consistent with

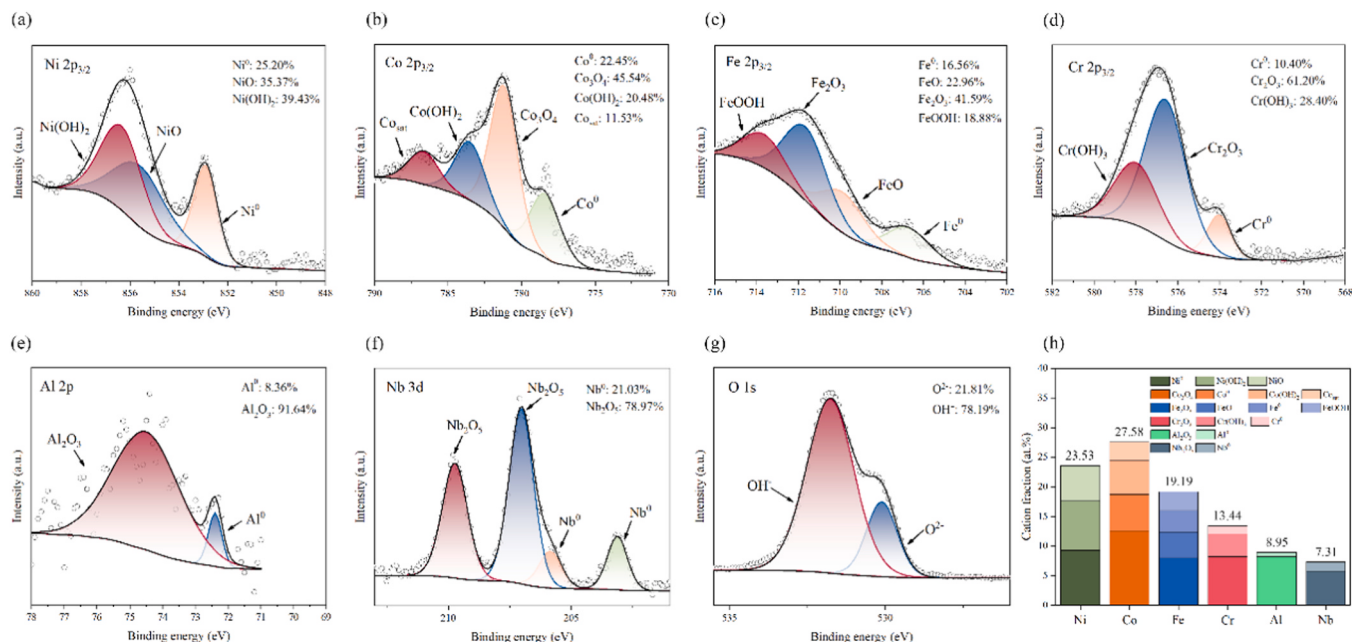


Fig. 6. XPS analysis of the passive film (potentiostatic polarization at 0.2 V_{SC} in 3.5 wt% NaCl solution for 2 h) on the Al4Nb4 alloy aged at 900 °C (FCC+D0₁₉ structure). High-resolution spectra of (a) Ni 2p_{3/2}, (b) Co 2p_{3/2}, (c) Fe 2p_{3/2}, (d) Cr 2p_{3/2}, (e) Al 2p, (f) Nb 3d, (g) O 1s. (h) Cationic fractions in the passive film, with their relative percentage marked.

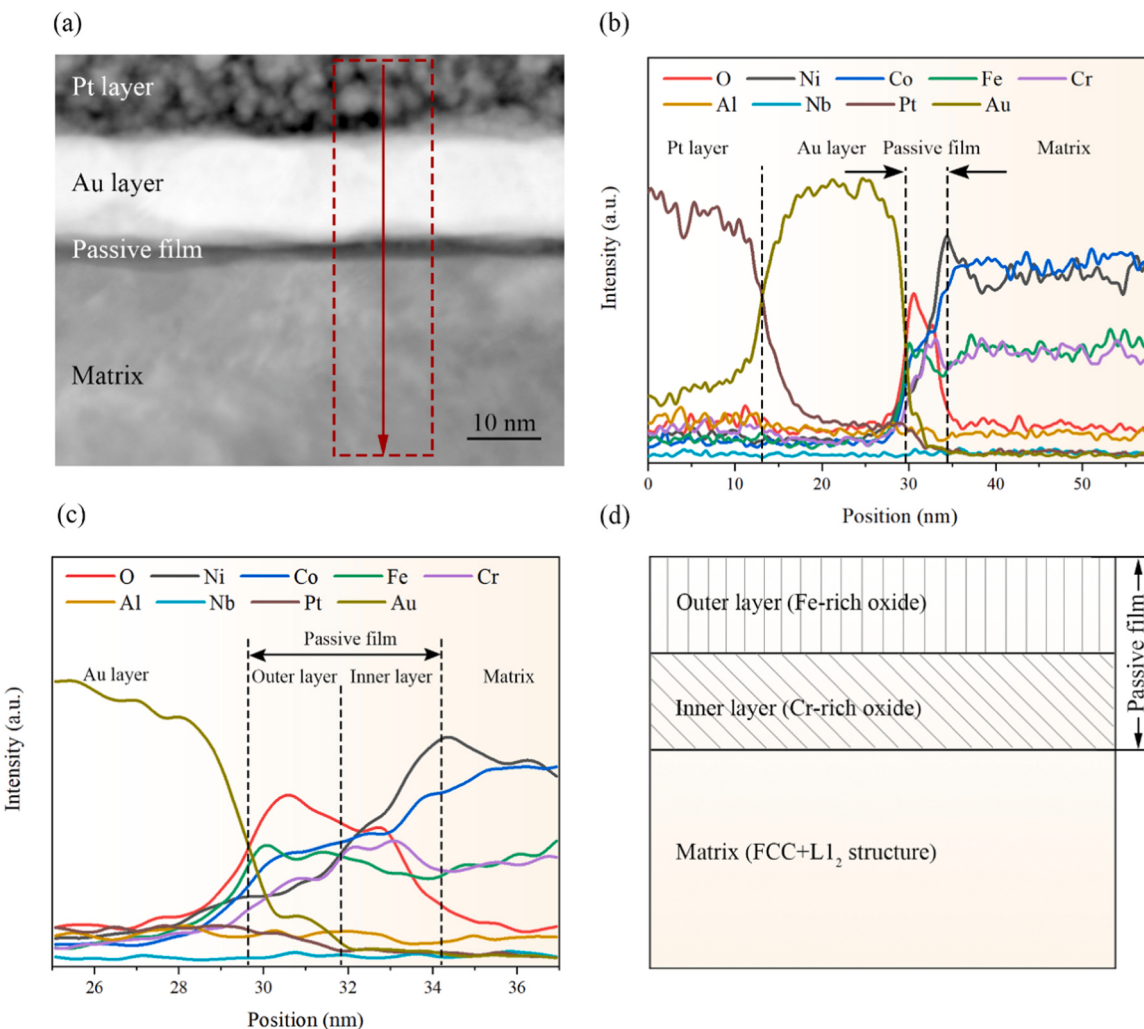


Fig. 7. STEM analysis of the passive film on the surface of L1₂-strengthened Al4Nb4 HEA. (a) Representative STEM image of the cross-sectional passive film, where four distinct layers can be observed, from top to bottom: Pt layer, deposited Au layer, passive film, and the matrix. (b) STEM line-scan profile along the red arrow in (a), demonstrating an oxygen-enriched protective passive film was formed. (c) Detailed line-scan analysis across the passive film, indicating the existence of a typical double-layer passive film, shown by the schematic diagram of (d), in which the inner layer is enriched in Cr and the outer layer is enriched in Fe.

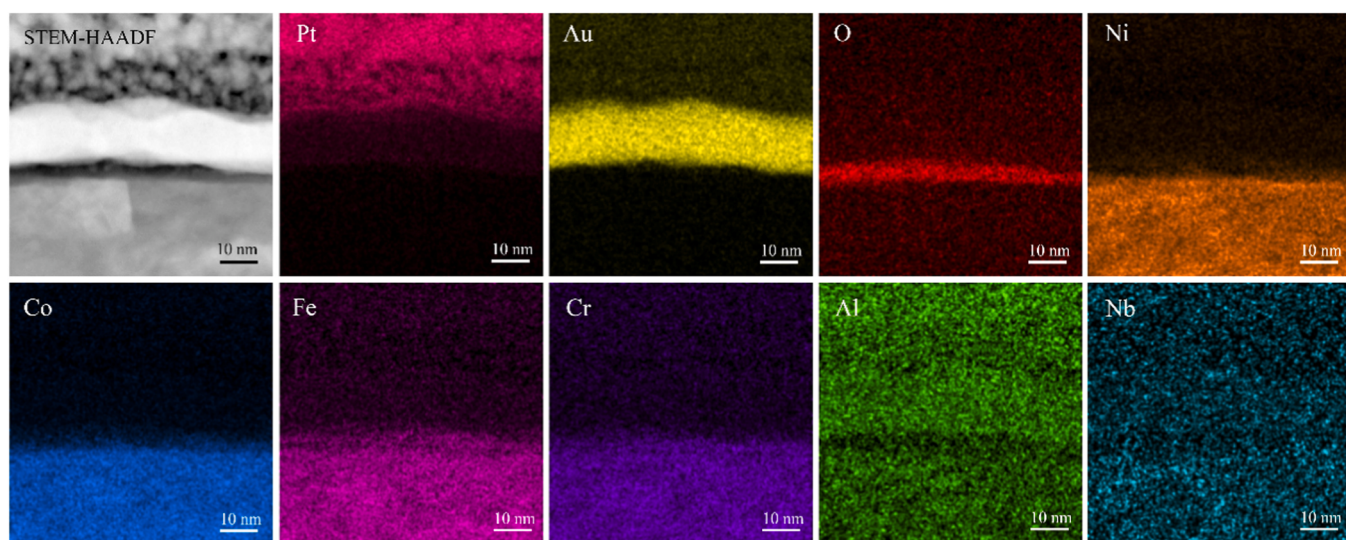


Fig. 8. STEM image of the L1₂-strengthened Al4Nb4 alloy surface passive film and the corresponding EDS maps for each element.

the general trends in the composition and structure of passive films reported previously in the literature [47,48]. The bilayer structure of the passive film has previously been widely accepted in traditional SS and recent HEAs through XPS depth profile or ion scattering spectroscopy, but has yet to be confirmed by STEM mapping due to the very thin nature of the passive film. For example, Calinski et al. obtained a quantitative profile of the surface passive layer on Fe-Cr alloy by ion scattering spectroscopy, and they found that the Cr : Fe ratio was not constant through the passive film thickness [47]. Due to the preferential dissolution of Fe in the aqueous environment, the inner layer of the surface passive film on the Fe-Cr alloy is enriched with Cr_2O_3 , Fe_2O_3 , and FeO , and the outer layer has a large amount of Fe_2O_3 accumulation. Dai et al. recently found that a double-layer passive film exists in Mo-containing FeCoNiCr HEAs by XPS depth profile, where the outer layer contains mixed Cr/Fe oxides and hydroxides, and the inner layer is mainly composed of Cr(III) species, *i.e.*, Cr_2O_3 [48]. Although these electron spectroscopy methods can provide a depth distribution of different constituent elements in the passive film, the thickness of which obtained by XPS depth profile, for example, has a significant error with the actual value, because it estimates the thickness based on the sputtering rate of the standard Ta_2O_5 film [49,50]. Another notable feature in Fig. 7(b) is the obvious enrichment of Ni at the interface between the passive film and the substrate, and based on the XPS results, it can be inferred that the enrichment here is metallic Ni (Ni^0). Further analysis

combined with STEM and XPS can confirm that the small amounts of Ni are present within the passive film mainly in the form of hydroxides, which is in good agreement with the compositional characteristics of passive films previously observed in Fe-Cr-Ni SS [51], Ni-based alloys containing Cr and Fe [52], and multi-component Cantor alloy [53].

The passive film structure formed on the L₁₂-strengthened HEA was further detected by aberration-corrected STEM techniques. Fig. 9 shows the atomic-resolution STEM-HAADF image of the potentiostatically grown passive film and the FFT patterns of the corresponding region (Au layer, passive film, and the alloy matrix). The bright and dark contrast in Fig. 9(a) is derived from the mass contrast originating from different elements contained in these regions. The intensity of the STEM-HAADF image is proportional to the atomic number of the element, so the passive film is imaged as dark contrast due to the high amount of light elements, such as O, contained in the passive film [54]. In contrast, the Au layer with a larger atomic number and the alloy matrix containing elements such as Ni and Co are imaged as bright and gray contrast, respectively. The FFT pattern from the passive layer demonstrates that the passive film is clearly differentiated from the crystalline structure of the alloy matrix and exhibits an amorphous structure. The large amount of oxides and hydroxides contained in the passive film tends to make it reach a relatively stable thermodynamic equilibrium state and promote the formation of an amorphous structure. Passive films with an amorphous structure have also been reported in other corrosion-resistant

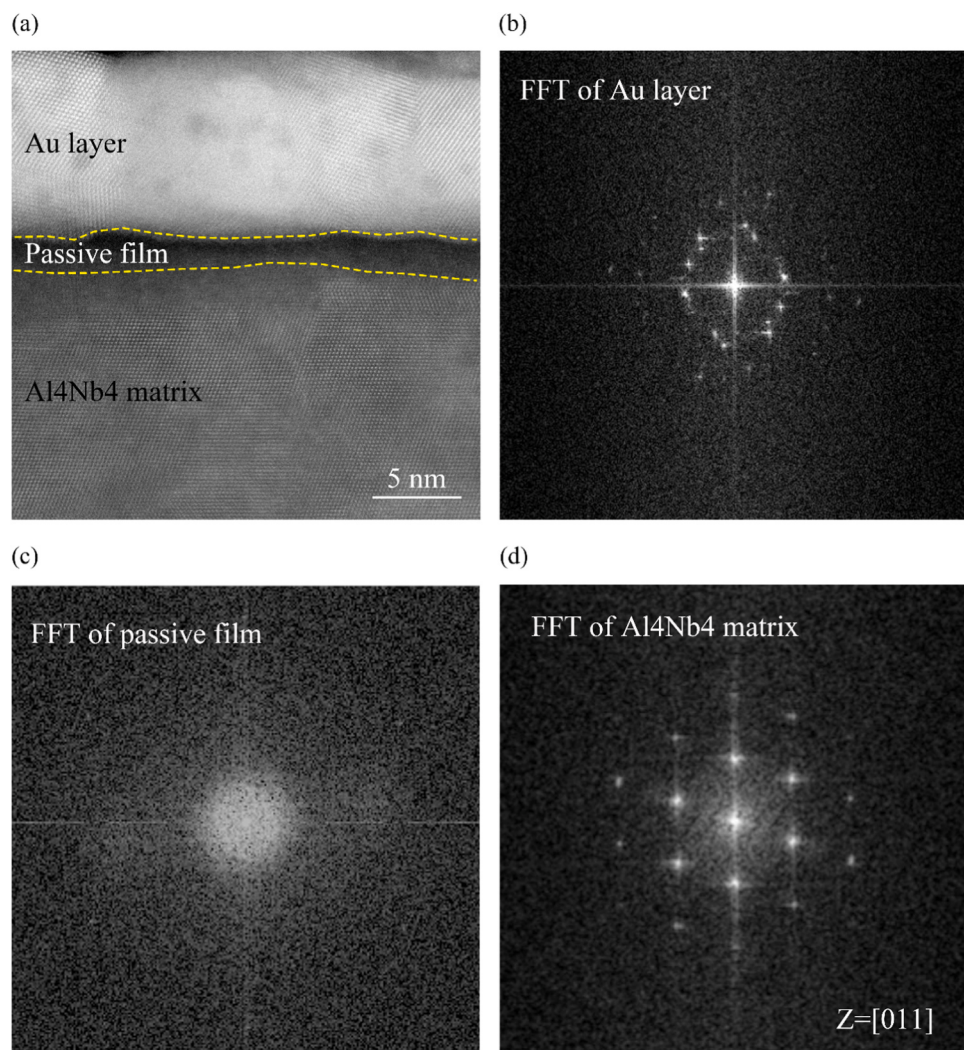


Fig. 9. (a) High-resolution STEM-HAADF image of the passive film formed on the surface of the L₁₂-strengthened Al4Nb4 HEA, with FFT patterns of the (b) deposited Au layer, (c) passive film, and (d) alloy matrix, showing the amorphous characteristics of the passive film.

alloys, and they generally have a higher resistance to corrosive ions (e.g., chloride ions) attacks than nanocrystalline passive films [55]. Such a duplex passive film with an amorphous structure on L1₂-strengthened Al4Nb4 HEA would indeed be favorable, attributed to its good bonding with the matrix and negligible electronic conductivity (high R_{ct} value).

3.5. Micro-galvanic corrosion and associated corrosion morphologies

The elemental partitioning of Al4Nb4 HEAs after aging treatment inevitably brings about localized micro-galvanic corrosion, which may affect the subsequent corrosion morphology. Fig. 10 shows the surface morphologies of single-phase FCC alloy, L1₂-strengthened alloy, and D0₁₉-strengthened alloy after potentiostatic polarization at 1 V_{SCE} (above the E_{pit}) for 3 minutes. Fig. 10(a, d, g) are the SEM images, Fig. 10(b, e, h) are the CLSM images, and the corresponding corrosion depth profiles along the blue dotted arrows in Fig. 10(b, e, h) are shown in Fig. 10(c, f, i). Single-phase FCC and L1₂-strengthened alloys exhibited typical pitting morphology, with a small number of pits observed in the single-phase FCC alloy and a large number of pits observed in the L1₂-strengthened alloy. Localized corrosion in the form of pitting is considered to be an autocatalytic process because the local environment is constantly acidified due to hydrolysis reactions of the dissolving metal cations [56]. The reactions that occur within a pit (considering a generic metal M) are



As a result, the metal inside the pits maintains a highly active dissolving state and reaches corrosion depths approaching ~100 μm due to the increasingly severe local environment compared to the bulk solution [1]. The effect of Ni, Al, and Nb-enriched L1₂ particles on the anodic polarization process is to increase the probability of metastable pitting, while the effect on the corrosion morphology is to increase the number of corrosion pits. Completely different corrosion phenomena were observed in the D0₁₉-strengthened alloy, manifesting as the IGC near grain boundaries and dealloying-like corrosion within the grains. Evidently, this unique corrosion morphology is caused by the continuous distribution of D0₁₉ particles on the grain boundaries and the lamellar D0₁₉ plates within the grains. It appears that the D0₁₉ phase acts as an electrochemically stable region, resulting in an anodic dissolution of the area around the D0₁₉ phase during the corrosion process, thereby causing the detachment of D0₁₉ particles at the grain boundaries (IGC) and the occurrence of intragranular dealloying.

To verify the micro-galvanic corrosion tendency in the D0₁₉-strengthened alloy, a simple immersion experiment combined with SKPFM testing was performed. The CLSM image after corrosion immersion tests in 2 M NaCl + 0.05 M HCl solution for 12 h is shown in Fig. 11(a), where the 0.05 M HCl was added to accelerate the corrosion kinetic process of the alloy. The corrosion depth profile along the blue arrow in Fig. 11(a) is depicted in Fig. 11(b), and it can be seen that the D0₁₉ phase is convex with respect to the surrounding FCC matrix after immersion. Fig. 12 further shows the SKPFM surface analysis of the D0₁₉-strengthened alloy. The AFM topography image (Fig. 12(a)) and 3D AFM map (Fig. S3) confirmed the electrochemical nobility of the lamellar D0₁₉ phase with respect to the FCC matrix. The corrosion

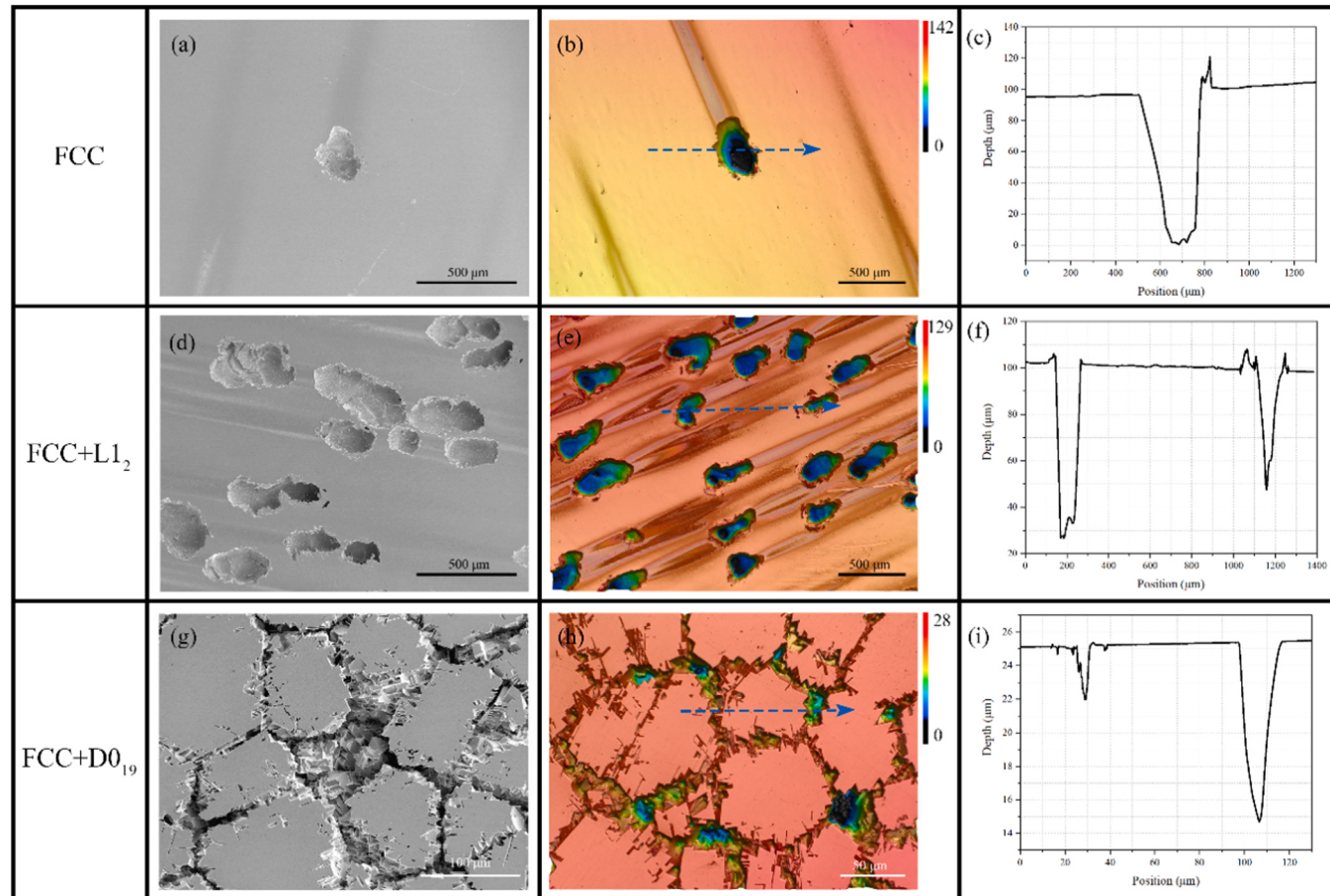


Fig. 10. Corrosion morphologies of Al4Nb4 HEAs after potentiostatic polarization at 1 V_{SCE} (above the E_{pit}) for 3 minutes. (a, d, g) SEM images and (b, e, h) CLSM images of single-phase FCC alloy, L1₂-strengthened alloy, and D0₁₉-strengthened alloy, respectively. (c, f, i) Depth profiles along the corresponding blue arrows in (b, e, h).

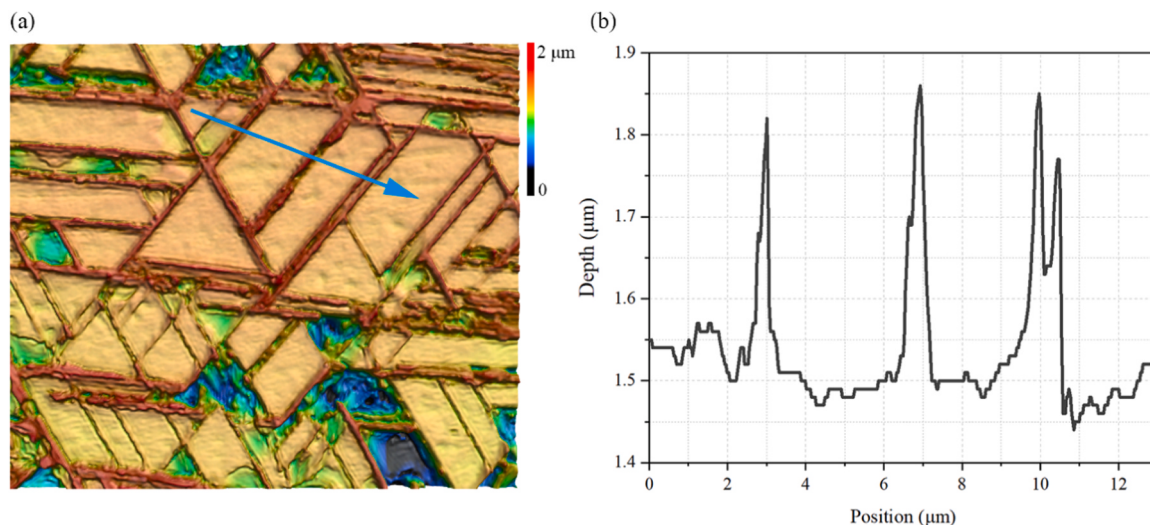


Fig. 11. (a) CLSM image of the D0₁₉-strengthened Al4Nb4 HEA after corrosion immersion testing in 2 M NaCl + 0.05 M HCl solution at 37 ± 0.5 °C for 12 h. (b) Depth profile along the blue arrow in (a), indicating the electrochemical nobility of D0₁₉ phase relative to the FCC matrix.

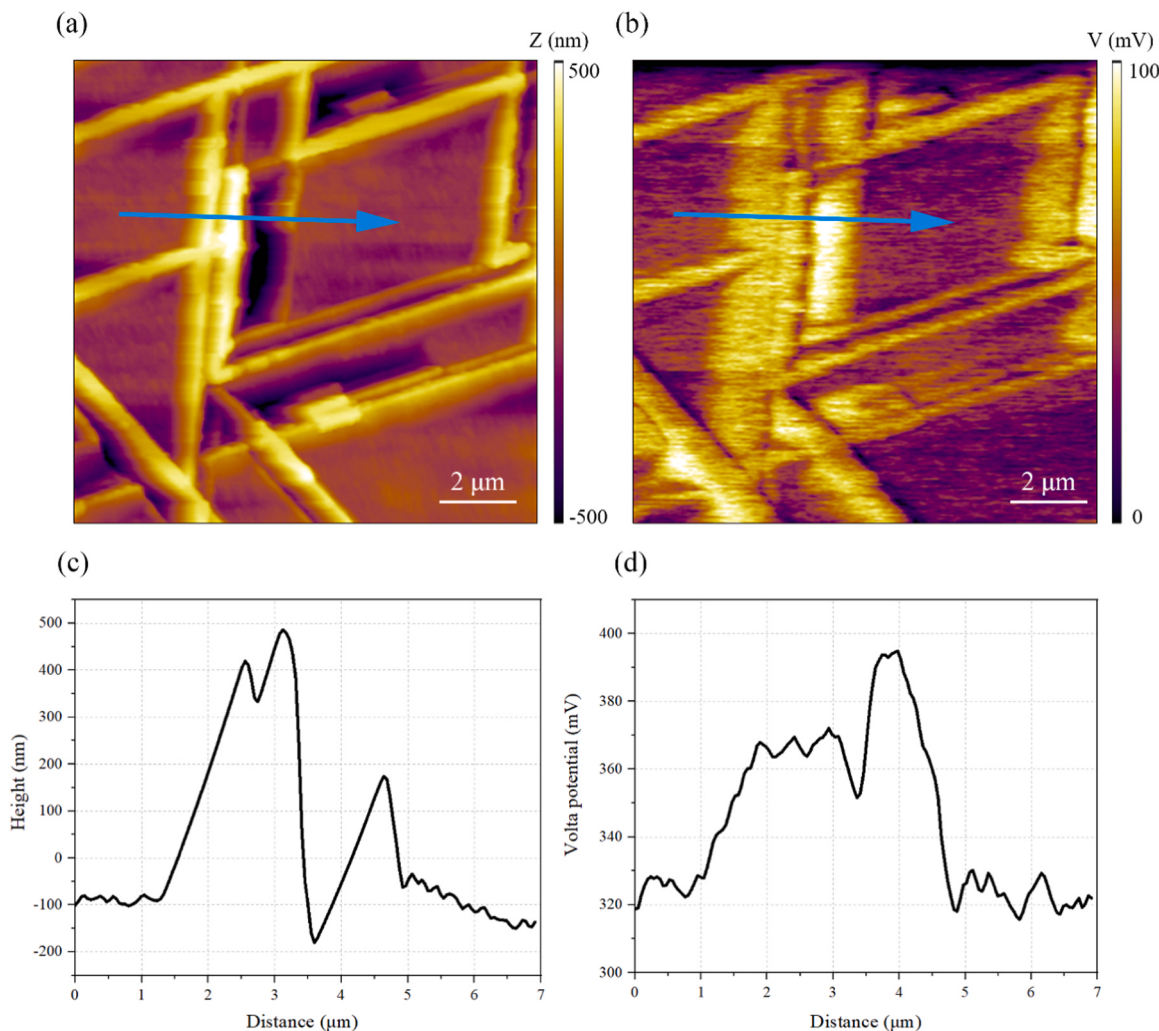


Fig. 12. SKPFM analysis of the D0₁₉-strengthened Al4Nb4 HEA. (a) AFM topography image and (b) Volta potential difference map. (c) Height fluctuations and (d) Volta potential differences along the blue arrows in (a) and (b), respectively. The pronounced potential difference between the D0₁₉ phase and FCC matrix suggests that severe localized micro-galvanic corrosion exists in the D0₁₉-strengthened HEA.

tendency between the two phases generally stems from the Volta potential difference caused by the different chemical compositions and structures, as shown in Fig. 12(b). The height fluctuations and Volta potential differences along the blue arrows in Fig. 12(a) and (b) are shown in Fig. 12(c) and (d), respectively, suggesting that the topographically protruding D0₁₉ phase has a higher Volta potential compared to the FCC matrix. The significant Volta potential difference between the two phases (~70 mV) is sufficient to cause severe micro-galvanic corrosion in the D0₁₉-strengthened alloy [57]. It has been reported that the Laves phase, which has a similar phase composition to the D0₁₉ phase, also has a higher Volta potential than the FCC matrix in Nb-containing FeCoNiCr HEAs, resulting in the preferential dissolution of the surrounding FCC matrix [58]. Therefore, the D0₁₉-strengthened alloy has the worst localized corrosion resistance compared to single-phase FCC and L1₂-strengthened counterparts, and its significant Volta potential fluctuation originated from the intense elemental partitioning behavior leads to its high susceptibility to IGC and micro-galvanic corrosion.

4. Conclusion

In this work, the electrochemical corrosion behavior of Al4Nb4 HEAs with different phase structures (*i.e.*, FCC, FCC+L1₂, FCC+D0₁₉) was systematically investigated in 3.5 wt% NaCl solution, and it was found that the temperature-dependent microstructural evolutions play an essential role in the aqueous corrosion performance and passive film features of the precipitation-strengthened HEAs. By combining TEM, APT, XPS, STEM mapping, atomic-scale STEM-HAADF, and SKPFM, some key conclusions can be drawn as follows:

- (1) Compared with the single-phase FCC alloy in the recrystallized state, the Al4Nb4 alloy aged at 700 °C and 900 °C is composed of FCC+L1₂ and FCC+D0₁₉ dual-phase structure, respectively. The nano-sized L1₂ particles are enriched with Ni, Al, and Nb, and the lamellar D0₁₉ phase is enriched with Ni and Nb. In these two HEAs with dual-phase structures, the orientation relationships between the precipitates and the FCC matrix are determined as <110>{111}_{L1₂}//<110>{111}_{FCC} and <1120>{0001}_{D0₁₉}//<110>{111}_{FCC}, respectively.
- (2) The elemental partitioning between the two phases leads to a slight decrease in the localized corrosion resistance of the L1₂-strengthened alloy compared to that of the single-phase FCC counterpart, and the D0₁₉-strengthened alloy has the worst localized corrosion resistance. Iron oxides and Cr₂O₃ species prevail in the passive films of single-phase FCC and L1₂-strengthened alloys, whereas a large amount of Ni, Co oxides and hydroxides are found in the passive films of D0₁₉-strengthened alloys. The increased proportion of hydroxides and the absence of bound water in the passive film make the D0₁₉-strengthened alloy highly vulnerable to corrosive ion attacks, leading to its inferior localized corrosion resistance.
- (3) A double-layer passive film with an outer Fe-rich layer and an inner Cr-rich layer was observed in the L1₂-strengthened alloy. The 3.5-nm-thick passive film is recognized as an amorphous structure with good adhesion to the matrix, which contributes to the excellent aqueous corrosion resistance of the L1₂-strengthened alloy.
- (4) Both the single-phase FCC and L1₂-strengthened alloys exhibit typical pitting morphology, and there are more pits in the L1₂-strengthened alloy. The intense elemental partitioning behavior and structural differences between the D0₁₉ phase and FCC matrix lead to unavoidable micro-galvanic corrosion of the D0₁₉-strengthened alloy, which changes the corrosion morphology and manifests itself as the IGC and intragranular dealloying-like corrosion. Based on such an in-depth and fundamental

understanding of the corrosion-mechanics-structure-composition relationship, new-type precipitation-strengthened HEAs with high strength, appreciable ductility, and superior corrosion resistance could be affordable in the future.

CRediT authorship contribution statement

J.Y. Zhang: Data curation, Conceptualization, Writing – original draft, Methodology. **Y.H. Zhou:** Investigation. **Z.Q. Ren:** Investigation. **J.H. Luan:** Investigation. **Y.L. Zhao:** Supervision. **T. Yang:** Supervision, Writing – original draft.

Declaration of Competing Interest

The authors declare that they have no competing financial interests or personal relationships that could have appeared to influence the work reported in this paper.

Data Availability

Data will be made available on request. All data in this work are available on request by contact with the corresponding author.

Acknowledgements

The authors are grateful for the financial support from the National Natural Science Foundation of China (Grant No. 52101135) and the Research Grants Council of the Hong Kong Special Administrative Region, China (Grant No. CityU 21205621).

Appendix A. Supporting information

Supplementary data associated with this article can be found in the online version at doi:10.1016/j.corsci.2024.112074.

References

- [1] M.P. Ryan, D.E. Williams, R.J. Chater, B.M. Hutton, D.S. McPhail, Why stainless steel corrodes, *Nature* 415 (6873) (2002) 770–774.
- [2] M.J. Duarte, J. Klemm, S.O. Klemm, K.J.J. Mayrhofer, M. Stratmann, S. Borodin, A. H. Romero, M. Madinehei, D. Crespo, J. Serrano, Element-resolved corrosion analysis of stainless-type glass-forming steels, *Science* 341 (6144) (2013) 372–376.
- [3] X. Li, D. Zhang, Z. Liu, Z. Li, C. Du, C. Dong, Materials science: Share corrosion data, *Nature* 527 (7579) (2015) 441–442.
- [4] D.D. Macdonald, Passivity—the key to our metals-based civilization, *Pure Appl. Chem.* 71 (6) (1999) 951–978.
- [5] H. Luo, S.S. Sohn, W. Lu, L. Li, X. Li, C.K. Soundararajan, W. Krieger, Z. Li, D. Raabe, A strong and ductile medium-entropy alloy resists hydrogen embrittlement and corrosion, *Nat. Commun.* 11 (1) (2020) 3081.
- [6] B. Kombaiah, Y. Zhou, K. Jin, A. Manzoor, J.D. Poplawsky, J.A. Aguiar, H. Bei, D. S. Aidiy, P.D. Edmondson, Y. Zhang, Nanoprecipitates to enhance radiation tolerance in high-entropy alloys, *ACS Appl. Mater. Interfaces* 15 (3) (2023) 3912–3924.
- [7] S. San, P. Adhikari, R. Sakidja, J. Brechtl, P.K. Liaw, W.-Y. Ching, Porosity modeling in a TiNbTaZrMo high-entropy alloy for biomedical applications, *RSC Adv.* 13 (51) (2023) 36468–36476.
- [8] K.Q. Yuan, Y. Jiang, S.C. Liu, X.Z. Li, S.S. Xu, X.X. Wu, Design of face-centered-cubic high entropy alloys with high strength and high toughness, *Rare Met. Mater. Eng.* 52 (11) (2023) 3981–4001.
- [9] J.Y. Zhang, B. Xiao, T. Chou, B. Cao, Y. Zhao, B. Liu, K. Huang, S. Yang, J. Su, Y. Liu, T. Yang, High-entropy alloys: a critical review of aqueous corrosion behavior and mechanisms, *High. Entropy Alloy. Mater.* (2023) 1–65.
- [10] L. Wei, W.-M. Qin, J.Y. Chen, W.-X. Lei, J.Y. Xi, L1₂-strengthened face-centered cubic high-entropy alloy with well pitting resistance, *Corros. Sci.* 215 (2023) 111043.
- [11] J.Y. Zhang, T. Chou, Y. Zhou, J. Luan, Y. Zhao, T. Yang, Corrosion-resistant L1₂-strengthened high-entropy alloy with high strength and large ductility, *Corros. Sci.* 225 (2023) 111593.
- [12] H. Cheng, H. Luo, X. Wang, X. Li, Microstructure and corrosion resistance properties of (FeCoNi)₈₆Al₇Ti₇ high-entropy alloy via different aging time, *Corros. Sci.* 226 (2024) 111670.
- [13] Y. Wang, G. Li, H. Li, Y. Mu, K. Sun, W. Zhao, D. Li, Y. Jia, G. Wang, Effect of aging on corrosion resistance of (FeCoNi)₈₆Al₇Ti₇ high entropy alloys, *Corros. Sci.* 227 (2024) 111717.

- [14] Y. Shi, B. Yang, X. Xie, J. Brecht, K.A. Dahmen, P.K. Liaw, Corrosion of Al_xCoCrFeNi high-entropy alloys: Al-content and potential scan-rate dependent pitting behavior, *Corros. Sci.* 119 (2017) 33–45.
- [15] B.Y. Li, P. Kun, A.P. Hu, L.P. Zhou, J.J. Zhu, D.Y. Li, Structure and properties of FeCoNiCrCu_{0.5}Al_x high-entropy alloy, *Trans. Nonferr. Met. Soc. China* 23 (2013) 735–741.
- [16] R. Wei, Z. Jiang, Q. Gao, C. Chen, K. Zhang, S. Zhang, Z. Han, T. Wang, S. Wu, F. Li, The effect of Co substitutions for Ni on microstructure, mechanical properties and corrosion resistance of Fe₅₀Mn₂₅Cr₁₅Ni₁₀ medium-entropy alloy, *Intermetallics* 149 (2022) 107654.
- [17] C.H. Tsau, C.Y. Yeh, M.C. Tsai, The effect of Nb-content on the microstructures and corrosion properties of CrFeCoNb_x high-entropy alloys, *Materials* 12 (22) (2019) 3716.
- [18] M. Zhang, X. Shi, Z. Li, H. Xu, G. Li, Corrosion behaviors and mechanism of CrFeNi₂ based high-entropy alloys, *Corros. Sci.* 207 (2022) 110562.
- [19] A.V. Ayyagari, B. Gwalani, S. Muskeri, S. Mukherjee, R. Banerjee, Surface degradation mechanisms in precipitation-hardened high-entropy alloys, *npj Mater. Degrad.* 2 (1) (2018) 33.
- [20] X. Yan, H. Guo, W. Yang, S. Pang, Q. Wang, Y. Liu, P.K. Liaw, T. Zhang, Al_{0.3}Cr_xFeCoNi high-entropy alloys with high corrosion resistance and good mechanical properties, *J. Alloy. Compd.* 860 (2021) 158436.
- [21] Z. Pan, H. Luo, Q. Zhao, H. Cheng, Y. Wei, X. Wang, B. Zhang, X. Li, Tailoring microstructure and corrosion behavior of CoNiAl_x medium entropy alloys via Al addition, *Corros. Sci.* 207 (2022) 110570.
- [22] X. Duan, T. Han, X. Guan, Y. Wang, H. Su, K. Ming, J. Wang, S. Zheng, Cooperative effect of Cr and Al elements on passivation enhancement of eutectic high-entropy alloy AlCoCrFeNi_{2.1} with precipitates, *J. Mater. Sci. Technol.* 136 (2023) 97–108.
- [23] J.Y. Zhang, B. Xiao, Q. Li, B. Cao, J. Hou, S. Liu, J. Zhang, W. Xiao, J. Luan, Y. Zhao, T. Yang, Temperature-dependent microstructural evolutions and deformation mechanisms of (Ni₂Co₂FeCr)₉₂Al₄Nb₄ high-entropy alloys, *J. Alloy. Compd.* 918 (2022) 165597.
- [24] B. Gault, M.P. Moody, F. De Geuser, G. Tsafnat, A. La Fontaine, L.T. Stephenson, D. Haley, S.P. Ringer, Advances in the calibration of atom probe tomographic reconstruction, *J. Appl. Phys.* 105 (3) (2009).
- [25] Y.L. Zhao, T. Yang, Y. Li, L. Fan, B. Han, Z. Jiao, D. Chen, C.T. Liu, J.J. Kai, Superior high-temperature properties and deformation-induced planar faults in a novel L₁-strengthened high-entropy alloy, *Acta Mater.* 188 (2020) 517–527.
- [26] S. Choudhary, K. Ogle, O. Gharbi, S. Thomas, N. Birbilis, Recent insights in corrosion science from atomic spectroelectrochemistry, *Electrochim. Sci. Adv.* 2 (6) (2022) e2100196.
- [27] E. McCafferty, Validation of corrosion rates measured by the Tafel extrapolation method, *Corros. Sci.* 47 (12) (2005) 3202–3215.
- [28] C. Punckt, M. Bolscher, H.H. Rotermund, A.S. Mikhailov, L. Organ, N. Budiansky, J.R. Scully, J.L. Hudson, Sudden onset of pitting corrosion on stainless steel as a critical phenomenon, *Science* 305 (5687) (2004) 1133–1136.
- [29] M. Li, R.K. Nutor, Q. Cao, X. Wang, S. Ding, D. Zhang, J.-Z. Jiang, Corrosion behavior of Al-containing CoNiV alloys, *Corros. Sci.* 207 (2022) 110567.
- [30] J. Wang, Z. Zhang, H. Dai, H. Fujiwara, X. Chen, K. Ameyama, Enhanced corrosion resistance of CoCrFeMnNi high entropy alloy using heterogeneous structure design, *Corros. Sci.* 209 (2022) 110761.
- [31] Y. Shi, L. Collins, R. Feng, C. Zhang, N. Balke, P.K. Liaw, B. Yang, Homogenization of Al_xCoCrFeNi high-entropy alloys with improved corrosion resistance, *Corros. Sci.* 133 (2018) 120–131.
- [32] D.D. Macdonald, Reflections on the history of electrochemical impedance spectroscopy, *Electrochim. Acta* 51 (8–9) (2006) 1376–1388.
- [33] H. Luo, S. Zou, Y.-H. Chen, Z. Li, C. Du, X. Li, Influence of carbon on the corrosion behaviour of interstitial equiatomic CoCrFeMnNi high-entropy alloys in a chlorinated concrete solution, *Corros. Sci.* 163 (2020) 108287.
- [34] H. Luo, Z. Li, A.M. Mingers, D. Raabe, Corrosion behavior of an equiatomic CoCrFeMnNi high-entropy alloy compared with 304 stainless steel in sulfuric acid solution, *Corros. Sci.* 134 (2018) 131–139.
- [35] C. Della Rovere, J. Alano, R. Silva, P. Nascente, J. Otubo, S. Kuri, Characterization of passive films on shape memory stainless steels, *Corros. Sci.* 57 (2012) 154–161.
- [36] A.J. Bard, L.R. Faulkner, H.S. White, *Electrochemical Methods: Fundamentals and Applications*, John Wiley & Sons, 2022.
- [37] K. Coldsnow, D. Yan, G.E. Paul, H. Torbati-Sarraf, B. Poorganji, O. Ertorer, K. S. Tan, S. Pasebani, S.A. Torbati-Sarraf, O.B. Isgr, Electrochemical behavior of alloy 22 processed by laser powder bed fusion (L-PBF) in simulated seawater and acidic aqueous environments, *Electrochim. Acta* 421 (2022) 140519.
- [38] M. Ameer, A.M. Fekry, F.E.T. Heikal, Electrochemical behaviour of passive films on molybdenum-containing austenitic stainless steels in aqueous solutions, *Electrochim. Acta* 50 (1) (2004) 43–49.
- [39] C.O. Olsson, D. Landolt, Passive films on stainless steels—chemistry, structure and growth, *Electrochim. Acta* 48 (9) (2003) 1093–1104.
- [40] J.W. Schultze, M. Lohrengel, Stability, reactivity and breakdown of passive films. Problems of recent and future research, *Electrochim. Acta* 45 (15–16) (2000) 2499–2513.
- [41] T. Misawa, K. Hashimoto, S. Shimodaira, The mechanism of formation of iron oxide and oxyhydroxides in aqueous solutions at room temperature, *Corros. Sci.* 14 (2) (1974) 131–149.
- [42] S. Haupt, H.-H. Strehblow, A combined surface analytical and electrochemical study of the formation of passive layers on FeCr alloys in 0.5 M H₂SO₄, *Corros. Sci.* 37 (1) (1995) 43–54.
- [43] Z. Wang, Y. Yan, Y. Wu, X. Huang, Y. Zhang, Y. Su, L. Qiao, Corrosion and tribocorrosion behavior of equiatomic refractory medium entropy TiZr(Hf, Ta, Nb) alloys in chloride solutions, *Corros. Sci.* 199 (2022) 110166.
- [44] X.H. Gu, H.J. Yan, Q.H. Zhang, X.Z. Meng, L.K. Wu, F.H. Cao, Microstructure characterization and corrosion behavior of Al_x(CoCrFeNi)_{100-x} (x = 0, 5, 10, 15, 20) high entropy alloys in 0.5 M H₂SO₄ solution, *J. Alloy. Compd.* 944 (2023) 169247.
- [45] J.R. Scully, S.B. Inman, A.Y. Gerard, C.D. Taylor, W. Windl, D.K. Schreiber, P. Lu, J. E. Saal, G.S. Frankel, Controlling the corrosion resistance of multi-principal element alloys, *Scr. Mater.* 188 (2020) 96–101.
- [46] G. Okamoto, Passive film of 18-8 stainless steel structure and its function, *Corros. Sci.* 13 (6) (1973) 471–489.
- [47] C. Calinski, H.H. Strehblow, ISS depth profiles of the passive layer on Fe/Cr alloys, *J. Electrochem. Soc.* 136 (5) (1989) 1328.
- [48] C. Dai, H. Luo, J. Li, C. Du, Z. Liu, J. Yao, X-ray photoelectron spectroscopy and electrochemical investigation of the passive behavior of high-entropy FeCoCrNiMo_x alloys in sulfuric acid, *Appl. Surf. Sci.* 499 (2020) 143903.
- [49] Q.T. Song, J. Xu, (TiZrNbTa)₉₀Mo₁₀ high-entropy alloy: Electrochemical behavior and passive film characterization under exposure to Ringer's solution, *Corros. Sci.* 167 (2020) 108513.
- [50] C. Nkoua, J. Esvan, B. Tribollet, R. Basseguy, C. Blanc, Combined electrochemical impedance spectroscopy and X-ray photoelectron spectroscopy analysis of the passive films formed on 5083 aluminium alloy, *Corros. Sci.* (2023) 111337.
- [51] V. Maurice, W. Yang, P. Marcus, , X-Ray photoelectron spectroscopy and scanning tunneling microscopy study of passive films formed on (100) Fe-18Cr-13Ni single-crystal surfaces, *J. Electrochem. Soc.* 145 (3) (1998) 909.
- [52] P. Marcus, J. Grimal, The anodic dissolution and passivation of NiCrFe alloys studied by ESCA, *Corros. Sci.* 33 (5) (1992) 805–814.
- [53] L. Wang, D. Mercier, S. Zanna, A. Seyeux, M. Laurent-Brocq, L. Perriere, I. Guillot, P. Marcus, Study of the surface oxides and corrosion behaviour of an equiatomic CoCrFeMnNi high entropy alloy by XPS and ToF-SIMS, *Corros. Sci.* 167 (2020) 108507.
- [54] Y. Xu, H. Jia, P. Gao, D.E. Galvez-Aranda, S.P. Beltran, X. Cao, P.M. Le, J. Liu, M. H. Engelhard, S. Li, Direct in-situ measurement of electrical properties of solid electrolyte interphase on lithium metal anode, *Nat. Energy* 8 (2023) 1345–1354.
- [55] B. Zhang, J. Wang, B. Wu, X. Guo, Y. Wang, D. Chen, Y. Zhang, K. Du, E. Oguzie, X. Ma, Unmasking chloride attack on the passive film of metals, *Nat. Commun.* 9 (1) (2018) 2559.
- [56] G.S. Frankel, J.D. Vienna, J. Lian, J.R. Scully, S. Gin, J.V. Ryan, J. Wang, S.H. Kim, W. Windl, J. Du, A comparative review of the aqueous corrosion of glasses, crystalline ceramics, and metals, *npj Mater. Degrad.* 2 (1) (2018) 15.
- [57] V. Guillaumin, P. Schmutz, G. Frankel, Characterization of corrosion interfaces by the scanning Kelvin probe force microscopy technique, *J. Electrochim. Soc.* 148 (5) (2001) B163.
- [58] X. Wen, X. Cui, G. Jin, Y. Liu, Y. Zhang, X. Zhang, E. Liu, H. Tian, Y. Fang, Corrosion and tribo-corrosion behaviors of nano-lamellar Ni_{1.5}Cr_{0.5}Mo_{0.1}Nb_x eutectic high-entropy alloy coatings: the role of dual-phase microstructure, *Corros. Sci.* 201 (2022) 110305.